

# Dynamic Activation of Adsorbed Intermediates via Axial Traction for the Promoted Electrochemical CO<sub>2</sub> Reduction

Xinyue Wang,<sup>[a]</sup> Yu Wang,<sup>[d]</sup> Xiahan Sang,<sup>[e]</sup> Wanzhen Zheng,<sup>[a]</sup> Shihan Zhang,<sup>\*[c]</sup> Shuai Ling,<sup>[b]</sup> Bin Yang,<sup>[a]</sup> Zhongjian Li,<sup>[a]</sup> Jianmeng Chen,<sup>[c]</sup> Lecheng Lei,<sup>[a]</sup> Nadia Mohd Adli,<sup>[f]</sup> Michael K. H. Leung,<sup>[g]</sup> Ming Qiu,<sup>\*[b]</sup> Gang Wu,<sup>\*[f]</sup> and Yang Hou<sup>\*[a,h]</sup>

- [a] X. Wang, W. Zheng, Dr. B. Yang, Dr. Z. Li, Prof. Dr. L. Lei, Prof. Dr. Y. Hou  
Key Laboratory of Biomass Chemical Engineering of Ministry of Education, College of Chemical and Biological Engineering, Zhejiang University  
Hangzhou 310027, China  
E-mail: yhou@zju.edu.cn
- [b] S. Ling, Prof. Dr. M. Qiu  
Institute of Nanoscience and Nanotechnology, College of Physical Science and Technology, Central China Normal University  
Wuhan 430079, China  
E-mail: qium@mail.ccnu.edu.cn
- [c] Prof. Dr. S. Zhang, Prof. Dr. J. Chen  
College of Environment, Zhejiang University of Technology  
Hangzhou 310027, China  
E-mail: shihanzhang@zjut.edu.cn
- [d] Dr. Y. Wang  
Shanghai Synchrotron Radiation Facility, Shanghai Institute of Applied Physics, Chinese Academy of Sciences  
Shanghai 201204, China
- [e] Prof. Dr. X. Sang  
Nanostructure Research Center, Wuhan University of Technology  
Wuhan 430070, China
- [f] Nadia Mohd Adli, Prof. Dr. G. Wu  
Department of Chemical and Biological Engineering, University at Buffalo, the State University of New York  
Buffalo, NY, 14260, United States  
E-mail: gangwu@buffalo.edu
- [g] Prof. Dr. Michael K. H. Leung  
Ability R&D Energy Research Centre, School of Energy and Environment, City University of Hong Kong  
Hong Kong, China
- [h] Dr. B. Yang, Dr. Z. Li, Prof. Dr. L. Lei, Prof. Dr. Y. Hou  
Institute of Zhejiang University - Quzhou  
Quzhou 324000, China

Supporting Information for this article is given via a link at the end of the document.

**Abstract:** Regulating the local environment and structure of metal center coordinated by nitrogen ligands (e.g., M-N<sub>4</sub>) to accelerate overall reaction dynamics of electrochemical CO<sub>2</sub> reduction reaction (CO<sub>2</sub>RR) has attracted extensive attention. Herein, we develop an axial traction strategy to optimize the electronic structure of M-N<sub>4</sub> moiety and construct atomically dispersed nickel sites coordinated with four nitrogen atoms and one axial oxygen atom, which are embedded within the carbon matrix (Ni-N<sub>4</sub>-O/C). The Ni-N<sub>4</sub>-O/C electrocatalyst exhibited excellent CO<sub>2</sub>RR performance with a maximum CO Faradic efficiency (FE) close to 100% at -0.9 V. The CO FE could be maintained above 90% in a wide range of potential window from -0.5 to -1.1 V. The superior CO<sub>2</sub>RR activity is due to the Ni-N<sub>4</sub>-O active moiety composed of a Ni-N<sub>4</sub> site with an additional oxygen ligand that induces an axial traction effect. The unique structure was evidenced by aberration-corrected scanning transmission electron microscopy and synchrotron radiation X-ray absorption spectroscopy. Theoretical calculations elucidate that the introduction of axial oxygen atom could optimize surface states of Ni-N<sub>4</sub> moieties and enhance the charge polarization effect, therefore decreasing the potential barrier of intermediate COOH\* formation, a key factor to accelerate the reaction kinetics and boost the CO<sub>2</sub>RR performance.

## Introduction

The electrochemical CO<sub>2</sub> reduction reaction (CO<sub>2</sub>RR) is one of the viable approaches to convert CO<sub>2</sub> into carbon monoxide efficiently (CO) or other value-added fuels. Because CO gas is an important raw material for Fischer-Tropsch synthesis in industrial productions, the CO production via CO<sub>2</sub>RR has received extensive attention.<sup>[1]</sup> However, this technology is still far from practical implementations due to the lack of high-performance catalysts to reduce energy consumption and increase CO selectivity.<sup>[2]</sup>

From the thermodynamics point of view, the standard redox reaction of the CO<sub>2</sub>RR to CO ( $E^0 = -0.11$  V vs. RHE) is close to the hydrogen evolution reaction (HER) ( $E^0 = 0$  V vs. RHE). Also, the CO<sub>2</sub>RR is significantly suppressed by the slow reaction kinetics, especially the electronation activating step, which changes the geometry of a highly stable linear CO<sub>2</sub> molecule to the energetically unstable \*CO<sub>2</sub><sup>-</sup> radical ion ( $E^0 = -1.90$  V vs. RHE) and further protonation to form an active intermediate.<sup>[3]</sup> Therefore, it is of significance to improve the main bottleneck of CO<sub>2</sub>RR reaction kinetics. Great efforts have been devoted to revealing and improving the critical CO<sub>2</sub> activation step; however, an understanding of active sites' nature from a dynamic perspective remains a grand challenge.<sup>[4]</sup>

The intermediate COOH\* is commonly believed to be an essential pathway for CO production. The energy barrier of COOH\* formation can be chosen as a vital descriptor that enables predicting the dynamic activation for the CO<sub>2</sub>RR.<sup>[5]</sup> Up to

now, several studies have reported that the COOH\* intermediate is favored to be stabilized on transition metal-nitrogen co-decorated nanocarbon (M-N-C) materials because the unfilled 3d orbitals could enhance the charge transfer between M center and COOH\* intermediate.<sup>[6]</sup> Considering that the catalytic performance of M-N-C materials for oxygen reduction reaction could take a further leap by rational modulation of the *d*-electron states of M centers via changing coordination environments,<sup>[7]</sup> in this regard, it called for a reasonable mean to increase the *d*-states of M sites to reduce the energy barrier of COOH\* formation and thus optimize the dynamic activation processes. Through analysis of typical biological substances with the structures of Fe-N<sub>5</sub> (cytochrome P450) and Fe-N<sub>4</sub>-Cl (chlorhematin),<sup>[8]</sup> the unique coordination formed between a metal and heterogeneous atoms over the parallelogram (M-N<sub>4</sub>) inspired us to develop an axial traction strategy via mimicking the biological structure. This axial traction strategy would optimize the coordination to improve the electronic structure of M-N<sub>4</sub> moiety and decrease the activation step's energy barriers. To our best knowledge, the axial traction effect in dynamics activation of CO<sub>2</sub>RR catalysis has never been investigated, and the corresponding catalytic mechanism is not reported yet.

Herein, we reported a novel CO<sub>2</sub>RR electrocatalyst consisting of atomically dispersed Ni-N<sub>4</sub> sites coordinated with an additional axial traction oxygen atom (Ni-N<sub>4</sub>-O/C). Due to unique electronic structure induced by the axial traction and a high surface area of 952 m<sup>2</sup> g<sup>-1</sup>, the Ni-N<sub>4</sub>-O/C exhibited remarkable CO<sub>2</sub>RR activity and selectivity, featured by a maximum Faradic efficiency (FE) of CO about 99.2% at -0.9 V with a turnover frequency (TOF) of 11,187 h<sup>-1</sup>. Further, the Ni-N<sub>4</sub>-O/C catalyst displayed an extraordinary wide potential window from -0.5 to -1.1 V with above 90% CO FE. The high CO FEs in such a wide potential range was not reported before on Ni-N<sub>x</sub> sites. The exceptional CO<sub>2</sub>RR performance of Ni-N<sub>4</sub>-O/C originates from the active center consisting of a Ni-N<sub>4</sub> moiety with axial oxygen traction, identified by aberration-corrected scanning transmission electron microscopy (AC-STEM) and X-ray absorption spectroscopy (XAS). The density functional theory (DFT) calculations further elucidated that the axial oxygen atom could efficiently modulate the single Ni site's electronic configurations in the Ni-N<sub>4</sub>-O/C structure. The axial traction effect enhances the electron transport property and decreases the free energy barriers of the CO<sub>2</sub>\* transition to COOH\* intermediate, thus boosting the reaction kinetics of the CO<sub>2</sub>RR.

## Results and Discussion

To study the effectiveness of the axial traction strategy, we firstly performed DFT calculations on parallelogram Ni-N<sub>4</sub> configuration with an oxygen atom (Figure 1 and Supporting Information, Figure S1). The oxygen atom was chosen mainly due to its larger electronegativity than the nitrogen atom, which was moderate enough and will not distort the parallelogram Ni-N<sub>4</sub> structure. The difference of electron density for COOH\* adsorption on the Ni-N<sub>4</sub> sites with and without axial oxygen traction was further examined. **Figure 1A** illustrated that axial traction of oxygen atom produced an electron-pushing effect, leading to more significant charge polarization on Ni-N<sub>4</sub>-O sites than Ni-N<sub>4</sub> sites. Accordingly, the surface states of Ni-N<sub>4</sub>-O/C were optimized to reduce the local work function and compared

to the Ni-N<sub>4</sub>/C. Consequently, the dynamic activation of Ni-N<sub>4</sub>-O/C for the CO<sub>2</sub>RR favors reducing the energy barrier of intermediate COOH\* formation in alkaline solution relative to the Ni-N<sub>4</sub>/C. Further analyses of the density of states (DOS) clarified that the introduction of an axial oxygen atom on Ni-N<sub>4</sub> structure could shift its Fermi level to the high-level and thus increase its total DOS around the Fermi level, especially the *d*-states of M atom (**Figure 1B**). Therefore, we predict that introducing an axial oxygen atom is a critical factor in optimizing the surface states of the Ni-N<sub>4</sub> center and enhancing the charge polarization effect, resulting in accelerated reaction kinetics and boosting the CO<sub>2</sub>RR catalysis significantly.

Inspired by DFT calculations, an atomically dispersed axial oxygen-coordinated Ni-N<sub>4</sub> moiety on a carbon matrix was prepared, as illustrated in **Figure 2A**. The Ni-N<sub>4</sub>-O/C precursor (Mn, Ni-MOFs) was firstly synthesized by using Mn-based metal-organic frameworks (Mn-MOFs) (Supporting Information, Figure S2) as active site host and then in-situ introduced nickel acetate as a guest (see details in Experimental Section). After further carbonization under ammonia atmosphere and acid leaching treatments, the O atom was anchored onto Ni-N<sub>4</sub> moiety within the carbon matrix (Supporting Information, Figures S3,4). The Mn species aggregated into MnO nanocrystals were completely

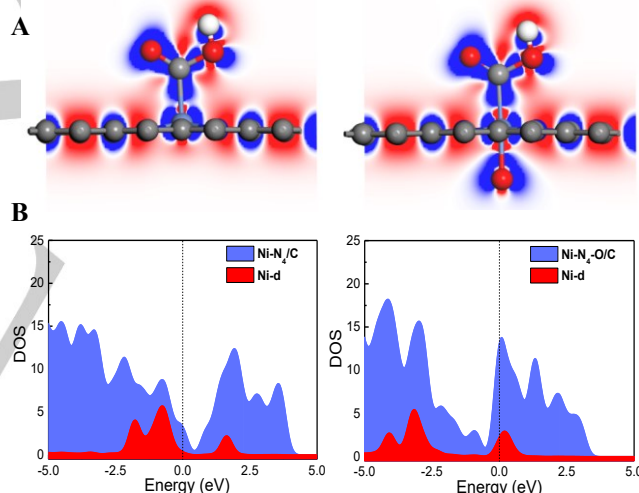


**Figure 1.** A) The difference of electron density for COOH\* intermediates adsorbed on Ni-N<sub>4</sub>/C and Ni-N<sub>4</sub>-O/C. B) Total DOS (blue-shaded areas) and *d*-states of Ni atom (red-shaded areas) in the optimized structures for Ni-N<sub>4</sub>/C and Ni-N<sub>4</sub>-O/C.

removed due to the abundance of O atoms around Mn atoms in Mn, Ni-MOFs precursor.<sup>[9]</sup> The possible chemical reaction during the formation of Ni-N<sub>4</sub>-O active sites was proposed in Supporting Information (Figure S5). The effect of carbonization temperatures and molar ratios of Mn: Ni salts on CO<sub>2</sub>RR activity were investigated, showing 700 °C, and a molar ratio of 4:1 are optimal (Supporting Information, Figures S6-9).

X-ray diffraction (XRD) patterns revealed the formation of graphitic carbon in the Ni-N<sub>4</sub>-O/C during the calcining process with the absence of metallic Ni species (Supporting Information, Figure S10). Based on the transmission electron microscopy (TEM) image, the Ni-N<sub>4</sub>-O/C displayed a bubble-like nanostructure with well-developed porosity (**Figures 2B,C**). No

significant nanocrystals or nanoparticles (NPs) were observed throughout the porous nanocarbon, which agrees with the selected area electron diffraction (SAED) observations (inset of Figure 2B). These results verified that the acid leaching treatment efficiently removed metallic Ni NPs and MnO nanocrystals. High-resolution TEM (HRTEM) images exhibited a lattice distance of 0.34 nm (Figure 2C), which was assigned to the (002) plane of partially graphitized carbon. The corresponding energy-dispersive X-ray spectroscopy (EDX) element mapping images demonstrated that the Ni-N<sub>4</sub>-O/C was comprised of Ni, N, O, and C elements, and all elements are uniformly distributed across the entire carbon supports (Supporting Information, Figure S11). Raman spectrum of Ni-N<sub>4</sub>-O/C displayed two peaks located at 1,342 and 1,586 cm<sup>-1</sup>, assignable to D band for defects/disorder, and G band for graphitic carbon. The *I<sub>D</sub>/I<sub>G</sub>* ratio of 2.1 for the Ni-N<sub>4</sub>-O/C was much higher than that of N-doped carbon (NC) (0.88), revealing the high density of defect sites due to the Ni anchoring (Supporting Information, Figure S12).

The X-ray photoelectron spectroscopy (XPS) survey of the Ni-N<sub>4</sub>-O/C further confirmed the co-existence of C, N, O, and Ni elements. However, the Ni's peak intensity was relatively weak due to its low concentration (Supporting Information, Figure S13). The Ni content in the Ni-N<sub>4</sub>-O/C is 0.37 wt.%, according to the coupled plasma optical emission spectrometry (ICP-OES) measurement. The high-resolution N 1s XPS spectrum of the Ni-N<sub>4</sub>-O/C could be divided into five peaks (Figure 2D). Four of them were typical peaks of N-doped carbons located at 398.2, 399.7, 400.7, and 402.3 eV, attributed to pyridinic N, pyrrolic N, graphitic N, and oxidized N, respectively.<sup>[10]</sup> The content of different N species was summarized in Supporting Information (Table S1). Notably, the peak centered at 399.2 eV corresponded to the N species coordinated with Ni atoms to form Ni-N<sub>x</sub> bonds.<sup>[11]</sup> Deconvoluted high-resolution O 1s XPS spectrum of the Ni-N<sub>4</sub>-O/C displayed the peak centered at 531.1 eV, which could be assigned to the Ni-bonded O formation (Figure 2E). Furthermore, the Ni-N<sub>4</sub>-O/C possessed a high Brunauer–Emmett–Teller (BET) surface area of 952 m<sup>2</sup> g<sup>-1</sup> and mesoporous features with a porous size around 4.0 nm (Supporting Information, Figure S14), which could enhance the mass transfer during the CO<sub>2</sub>RR.<sup>[12]</sup>

The electrocatalytic CO<sub>2</sub>RR performance of the Ni-N<sub>4</sub>-O/C was assessed in a CO<sub>2</sub>-saturated 0.5 M KHCO<sub>3</sub> solution using an H-type three-electrode cell. An on-line gas chromatograph (GC) and off-line <sup>1</sup>H nuclear magnetic resonance (<sup>1</sup>H NMR) were applied to analyze gaseous and liquid reduction products. No trace of liquid products was detected during the investigated potentials (Supporting Information, Figure S15). All potentials in this work were versus the reversible hydrogen electrode (RHE). The Ni-N<sub>4</sub>/C (Supporting Information, Figures S16-19) and NC (Supporting Information, Figures S20,21) without metallic Ni species were chosen as control samples. Notably, compared to Ni-N<sub>4</sub>/C and NC, the Ni-N<sub>4</sub>-O/C delivered a smaller onset potential of ~300 mV and generated the highest current density at all the applied potential (Figure 3A and Supporting Information, Figure S22). It demonstrated that the axial O atom plays a promotional role in boosting the CO<sub>2</sub>RR. The CO partial current density (*j<sub>CO</sub>*) of the Ni-N<sub>4</sub>-O/C was calculated based on CO FEs at different potentials (Supporting Information, Figure S23). The *j<sub>CO</sub>* value of the Ni-N<sub>4</sub>-O/C was up to 23 mA cm<sup>-2</sup> at -0.9 V

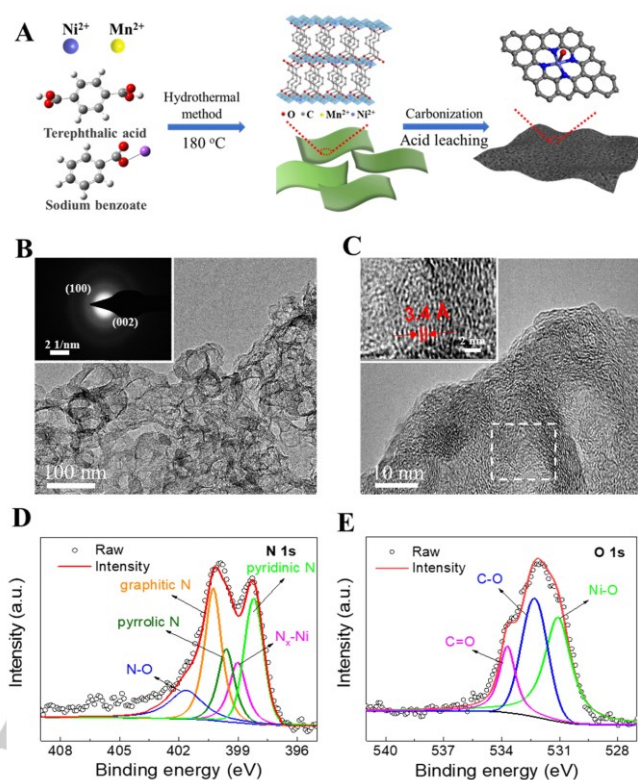


**Figure 2.** A) Schematic illustration of the synthesis process. B) TEM image, C) HRTEM image, D) high-resolution N 1s, and E) O 1s XPS spectra of Ni-N<sub>4</sub>-O/C. Inset B): SAED pattern; Inset C): enlarged HRTEM image.

with a maximum CO FE of 99.2%, which was much higher than those of control samples at the same applied potential (CO FE of 76% for Ni-N<sub>4</sub>/C with *j<sub>CO</sub>* of 6.0 mA cm<sup>-2</sup>, and CO FE of 30% for NC with *j<sub>CO</sub>* of 1.2 mA cm<sup>-2</sup>). When further normalizing the *j<sub>CO</sub>* of the Ni-N<sub>4</sub>-O/C by using its electrochemical surface area (ECSA), the specific CO<sub>2</sub>RR activity of the Ni-N<sub>4</sub>-O/C still higher than those of the Ni-N<sub>4</sub>/C and the NC. These comparisons further demonstrated that the axial traction of O atom significantly improved the activity of Ni-N<sub>4</sub>-O/C for the CO<sub>2</sub>RR (Figure 3B and Figures S24,25). Assuming that all surface Ni species acted as active sites, the Ni-N<sub>4</sub>-O/C's TOF was calculated to be 11,187 h<sup>-1</sup> at -0.9 V (Supporting Information, Figure S26). Notably, the Ni-N<sub>4</sub>-O/C displayed CO FEs of above 90% in a wider potential window than all of the previously reported Ni-N<sub>x</sub> catalysts (Figures 3C and Supporting Information, Table S2).<sup>[13]</sup> The traditional Ni-N<sub>4</sub>-C catalysts displayed CO FEs above 90% only in a potential window from -0.5 to -0.9 V. The N<sub>4</sub>-O/C catalyst can operate from -0.5 to -1.1 V with CO selectivity of above 90% (Supporting Information, Figure S27). Besides, a Tafel slope of 110 mV dec<sup>-1</sup> was determined for the Ni-N<sub>4</sub>-O/C (Figure 3D), which was between the single e<sup>-</sup> transfer to the adsorbed CO<sub>2</sub> molecules (118 mV dec<sup>-1</sup>) and subsequent formation of COOH\* intermediate (59 mV dec<sup>-1</sup>).<sup>[2, 14]</sup> Compared to the Ni-N<sub>4</sub>/C, the lower Tafel slope of the Ni-N<sub>4</sub>-O/C suggests that the favorable activation step of CO<sub>2</sub>\* to COOH\* is attributable to the axial oxygen atom. The fast activation kinetics of Ni-N<sub>4</sub>-O/C was further supported by electrochemical impedance spectroscopy (EIS) (Supporting Information, Figure S28). The smaller impedance of the Ni-N<sub>4</sub>-O/C than that of the Ni-N<sub>4</sub>/C and the NC indicated a low charge transfer resistance of

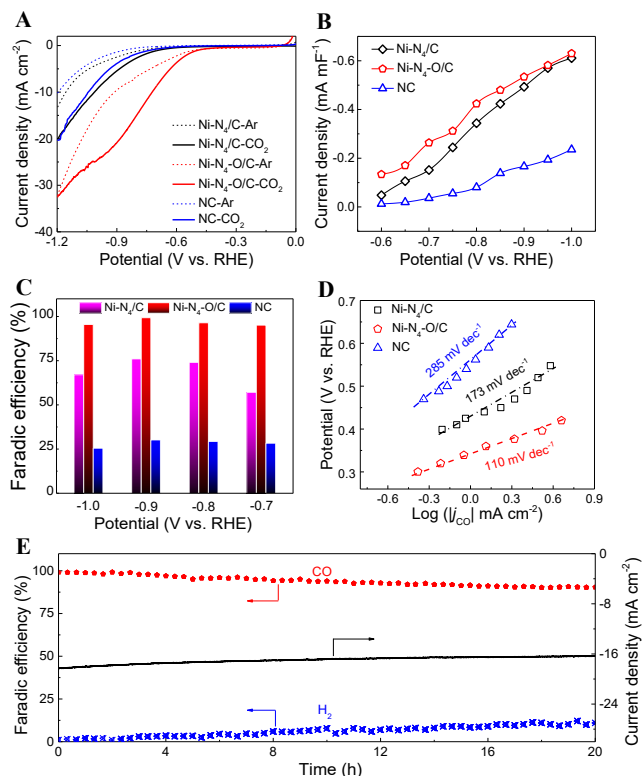


**Figure 3.** A) Polarization curves of Ni-N<sub>4</sub>-O/C (red), Ni-N<sub>4</sub>/C (black), and NC (blue) in CO<sub>2</sub>-saturated (Solid) and Ar-saturated (Dash) 0.5 M KHCO<sub>3</sub> solutions. B) Corresponding normalized  $j_{CO}$  to ECSA. C) CO FEs at different potentials for Ni-N<sub>4</sub>-O/C, Ni-N<sub>4</sub>/C, and NC. D) Corresponding Tafel slopes. E) Plot of current density and CO FE of Ni-N<sub>4</sub>-O/C for 20-hours at -0.9 V.

the CO<sub>2</sub>RR on the Ni-N<sub>4</sub>-O/C. Thus, the boosted CO<sub>2</sub>RR performance of the Ni-N<sub>4</sub>-O/C stemmed from the optimized reaction dynamics and facilitated charge transfer due to the introduction of an axial oxygen atom to the Ni-N<sub>4</sub> site. In addition to the high CO<sub>2</sub>RR activity and selectivity, the Ni-N<sub>4</sub>-O/C also showed encouraging stability during a 20-hour test, demonstrating CO FEs around 90% (Figure 3E). Notably, although no apparent changes in the morphology and structure were observed (Supporting Information, Figures S29,30), the percentage of Ni-O bonds of the aged Ni-N<sub>4</sub>-O/C slightly decreased after the 20-hour test (Supporting Information, Figure S31), implying that the O atom detached from the Ni-N<sub>4</sub> site.

AC-STEM measurements were conducted (Figures 4A, B) to determine the atomically dispersed Ni species in the Ni-N<sub>4</sub>-O/C catalyst. The contrast of bright spots was different from the surrounding elements. The atomic diameter of ~0.21 nm was very close to a single Ni atom, demonstrating that the Ni species were in the form of dispersed Ni atoms rather than Ni clusters. To further investigate the coordination environment of atomic Ni species, XAS analyses of the Ni-N<sub>4</sub>-O/C were performed. Ni foil, NiO, and nickel phthalocyanine (NiPc) were chosen as references. As shown in Figure 4C, X-ray absorption near edge structure (XANES) spectra revealed that the pre-edge features of the Ni-N<sub>4</sub>-O/C were close to that of the NiO and NiPc but not completely consistent, indicating a partial oxidation state of the Ni species in the Ni-N<sub>4</sub>-O/C.<sup>[15]</sup> Also, the transition of Ni 1s to 4p<sub>z</sub> orbital as a fingerprint of the square-planar NiPc (around 8,340 eV)<sup>[6b]</sup> was weak in the Ni-N<sub>4</sub>-O/C, implying that the Ni-N<sub>4</sub>-O/C

catalyst was not a typical square-planar M-N<sub>4</sub> model. Likely, the Ni-N<sub>4</sub> structure was partially distorted due to an additional heteroatom ligand such as O. Furthermore, Fourier transforms for extended X-ray fine structure (EXAFS) measurement of the Ni-N<sub>4</sub>-O/C was conducted. In Figure 4D, the Ni-Ni scattering path's vanishing at ~2.2 Å further suggested the atomic-level dispersion of the Ni species rather than the crystalline metal structure in the Ni-N<sub>4</sub>-O/C. Meanwhile, the control NiPc displayed a main peak at around 1.47 Å corresponding to Ni-N bonds, and the Ni-O exhibited the longer Ni-O scattering path at around 1.68 Å. The dominant peak center in the Ni-N<sub>4</sub>-O/C was around 1.52 Å that was between Ni-N and Ni-O scattering paths. The EXANES wavelet transform (WT-EXANES) of the Ni-N<sub>4</sub>-O/C was further performed (Figure 4E), allowing more intuitive comparisons on the radial distance k-space resolution.<sup>[16]</sup> The Ni-N<sub>4</sub>-O/C exhibited one intensity maximum at ~5 Å<sup>-1</sup>, which is closed to NiPc and moving toward NiO, but quite distinct from that in Ni foil (~8 Å<sup>-1</sup>). Therefore, the Ni species was further confirmed as atomically dispersed and co-coordinated with N and O atoms simultaneously. To further clarify the chemical environments of atomic Ni dispersion, the EXAFS curve-fitting analysis of the Ni-N<sub>4</sub>-O/C was performed to obtain the quantitative structural parameters around central atoms (Figure 4F and Supporting Information, Figure S32), and the obtained parameters were listed in Table S3. The optimal fitting results of the Ni-N<sub>4</sub>-O/C showed that the prominent peak of 1.47 Å was superimposed by four Ni/N/C with 2.07 Å and one Ni/O/N with 2.24 Å bond length, probably forming Ni/N/C<sub>4</sub> and an axial Ni-O/N bonds, respectively. Further O K-edge XAS results of the Ni-N<sub>4</sub>-O/C provided the foremost evidence for the presence of the Ni-O bond (Supporting Information, Figure S33). Moreover, instead of Ni-N<sub>5</sub>, an additional Ni-O bond in the Ni-N<sub>4</sub>-O/C was also supported by DFT calculations (Supporting Information,

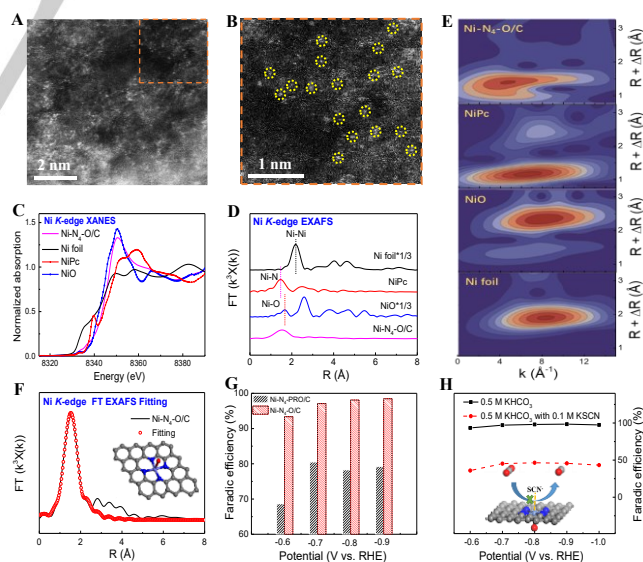


**Figure 4.** A-B) Atomic-resolution AC-STEM image and corresponding enlarged AC-STEM image. Atomic-level dispersed Ni species displaying in the form of the bright dots highlighted by yellow circles. C-D) Ni K-edge XANES and EXAFS spectra with reference samples of Ni foil, NiO, and NiPc. E) WT-EXANES of Ni-N<sub>4</sub>-O/C, Ni foil, NiO, and NiPc. F) EXAFS fitting curves in R space. Inset: corresponding schematic model of Ni-N<sub>4</sub>-O/C. G) The comparison of CO FEs of Ni-N<sub>4</sub>-PRO/C and Ni-N<sub>4</sub>-O/C. H) CO FEs of Ni-N<sub>4</sub>-O/C with and without 0.1 M SCN<sup>-</sup> ions, inset: illustrations of proposed poisoning model.

Figure S34), showing the lower formation energy of the Ni-N<sub>4</sub>-O structure. Therefore, based on AC-STEM, EXAFS, EXANES, and DFT calculations, we can conclude that the isolated Ni site is in the form of a Ni-N<sub>4</sub> configuration with Ni-O axial bond (inset of Figure 4F).

A control sample with partial removal of axial O atom was synthesized to reveal the promotional role of the axial Ni-O bond by heating the Ni-N<sub>4</sub>-O/C under H<sub>2</sub> atmosphere at 400 °C for two h (see details in Supporting Information), donated as Ni-N<sub>4</sub>-PRO/C. The element contents of Ni-N<sub>4</sub>-O/C before and after H<sub>2</sub> treatments, as quantified by XPS spectra, revealed that the ratio of C/N for Ni-N<sub>4</sub>-PRO/C was no apparent change. However, its ratio of C/O was significantly increased from 11.5 to 16.6 (Supporting Information, Figure S35), suggesting partial removal of axial O atoms. This was further supported by EDX element mapping results (Supporting Information, Figure S36). Notably, with the decrease of the O atoms content, the CO<sub>2</sub>RR activity of the Ni-N<sub>4</sub>-PRO/C was significantly declined (Figure 4G). The comparison further verified that the axial O atom traction is a key to boosting CO production.

To further discover the intrinsic active sites and reaction mechanisms of the Ni-N<sub>4</sub>-O/C, thiocyanate ions (SCN<sup>-</sup>) were added in electrolytes as an inhibitor to block the Ni-N<sub>4</sub> sites. Their CO FEs of both the Ni-N<sub>4</sub>-O/C and the Ni-N<sub>4</sub>/C were significantly declined (Figure 4H and Supporting Information, Figures S37,38). There was no apparent response to SCN<sup>-</sup> ions for the control NC sample (Supporting Information, Figure S39). This further validates that Ni-N<sub>4</sub> moieties in the Ni-N<sub>4</sub>-O/C and Ni-N<sub>4</sub>/C catalysts are active sites for the CO<sub>2</sub>RR. Notably, the blocking effect of SCN<sup>-</sup> ions for the Ni-N<sub>4</sub>/C was greater than Ni-N<sub>4</sub>-O/C. Likely, the axial O atom traction in Ni-N<sub>4</sub>-O/C was not easily poisoned because axial O atoms impeded the adsorption of SCN<sup>-</sup> ions.<sup>[17]</sup> The reduced CO<sub>2</sub>RR activity could be due to the blocking of SCN<sup>-</sup> ions on the opposite side of the axial O atom. Thus, CO<sub>2</sub> adsorption occurs at the opposite side of the axial O atom (the insert in Figure 4H).

Correlative theoretical calculations were further carried out using DFT calculations to understand the origins of the high CO<sub>2</sub>RR performance of the Ni-N<sub>4</sub>-O/C. The Ni-N<sub>x</sub>-O (x = 1, 2, 3, and 4) and Ni-N<sub>4</sub> moiety doped on carbon planes (denoted as Ni-N<sub>x</sub>-O/C and Ni-N<sub>4</sub>/C, respectively) models were constructed and geometrically optimized for CO<sub>2</sub>RR and water dissociation calculations. For revealing the CO<sub>2</sub>RR mechanism, the free energy profiles of the CO<sub>2</sub>RR on the Ni-N<sub>x</sub>-O/C (x = 1, 2, 3, and 4) and the Ni-N<sub>4</sub>/C models in a weak alkaline electrolyte (pH = 7.3) without applying electrode potential (U = 0) were provided (Supporting Information, Figure S40). The effect of electrode potentials and the solvent effects were also investigated and displayed in Supporting Information, Figures S41,42.<sup>[11]</sup> Furthermore, to determine the difficulty degree of CO<sub>2</sub>RR reaction more realistically, the potential barriers of transition states of each reaction step have been calculated (Figures 5A, B). For Ni-N<sub>1</sub>-O, Ni-N<sub>2</sub>-O, Ni-N<sub>3</sub>-O, and Ni-N<sub>4</sub>-O models, the potential barriers are 0.76, 0.71, 0.05, and 0.08 eV from the CO<sub>2</sub>\* transition to COOH\*, respectively, which likely is the rate-determining step. From the COOH\* transition to CO\*, the potential barriers are 0.16, 0.63, 1.77, and 1.86 eV on the four models, respectively. Thus, the desirable Ni-N<sub>4</sub>-O model has the highest barriers to form CO\*. These simulations indicate that an axial oxygen atom can affect the lengths of Ni-N bonding, population distributions of active center atoms, and the

adsorptions of intermediate states. The optimal surface states may change the CO<sub>2</sub>RR critical steps of these models. As commonly known, the water dissociation process also plays a crucial role in affecting CO<sub>2</sub>RR in the weak alkaline solution.<sup>[18]</sup> Thus, the potential barriers of transition states (Figure 5C) and the free energy profiles of water dissociation (Supporting Information, Figure S43) for the Ni-N<sub>x</sub>-O/C (x = 1, 2, 3, 4) and the Ni-N<sub>4</sub>/C models were also conducted. As shown in Figure 5C, during the water dissociation process, the barrier potentials from the H<sub>2</sub>O\* transition to H\* are 1.15, 1.19, 2.84, and 1.20 eV for Ni-N<sub>1</sub>-O, Ni-N<sub>2</sub>-O, Ni-N<sub>3</sub>-O, and Ni-N<sub>4</sub>-O models, respectively. The Ni-N<sub>4</sub>-O site can efficiently dissociate H<sub>2</sub>O and provide the proton for the CO<sub>2</sub>\* transition to COOH\*. Combined with the free energies results, the Ni-N<sub>4</sub>-O model has the best catalytic performance among all the investigated models. This result further illustrates the advantage of axial oxygen traction in the dynamic activation of CO<sub>2</sub> molecules during the reaction. Furthermore, the structural evolution of electrochemical CO<sub>2</sub>RR for the Ni-N<sub>4</sub>-O/C was also proposed in Figures 5D-G. The CO<sub>2</sub> molecules reacted on the back of graphene instead of the side containing O atoms, which is different from the traditional Ni-N<sub>4</sub>/C catalysts.

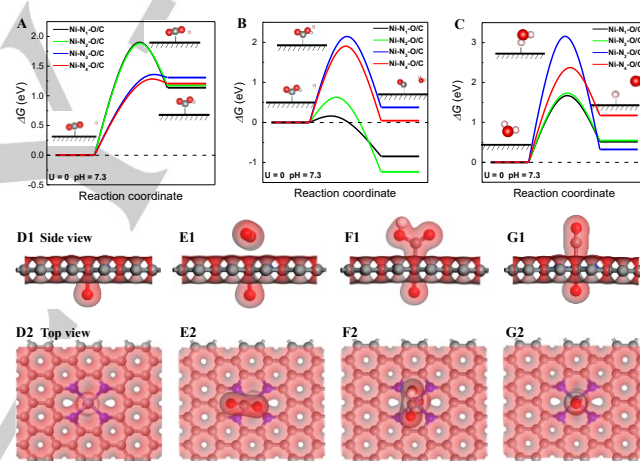


**Figure 5.** DFT-based potential barriers for the optimized Ni-N<sub>x</sub>-O/C (x = 1, 2, 3, and 4) models from the CO<sub>2</sub>\* transition to COOH\* (A), from the COOH\* transition to CO\* (B) during the CO<sub>2</sub>RR, and from the H<sub>2</sub>O\* transition to H\* during the water dissociation process (C). Structural evolution of electrochemical CO<sub>2</sub>RR for Ni-N<sub>x</sub>-O/C, (D1-G1) side view and (D2-G2) top view (Ni: cyan, N: blue, O: red, H: white and C: gray).

## Conclusion

In summary, we developed an axial traction strategy to construct an efficient nanocarbon CO<sub>2</sub>RR electrocatalyst composed of atomically dispersed Ni sites coordinated with four N atoms and one axial O atom. Owing to the atomic-level dispersion and large BET surface area, the Ni-N<sub>4</sub>-O/C exhibited prominent CO<sub>2</sub>RR activity with the maximum CO FE of 99.2% at around -0.9 V. It maintained high CO Fes above 90% in an extensive window from -0.5 to -1.1 V. The superior CO selectivity far outperformed other atomically dispersed Ni-N<sub>x</sub> sites embedded within carbon catalysts. The impressive CO<sub>2</sub>RR performance of the Ni-N<sub>4</sub>-O/C was attributed to the introduced axial O atom and atomically dispersed Ni-N<sub>4</sub> active sites, which were confirmed by extensive structural characterization. Theoretical calculations predicted

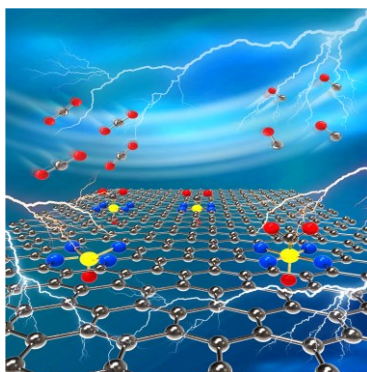
that the introduction of axial O atoms on the Ni-N<sub>4</sub> structure could optimize the surface states of Ni-N<sub>4</sub> moieties, enhance charge polarization effect, and reduce the reaction barriers of CO<sub>2</sub>\* to COOH\* as the limiting step, thus promoting the kinetic activation process and boosting the CO<sub>2</sub>RR activity. The axial traction strategy presented in this work may provide a new strategy to design a series of unique M-N<sub>4</sub>-X (X = O, S, Cl, etc.) catalysts with optimal electronic structures for various electrochemical reactions, such as hydrogen evolution, oxygen reduction,<sup>[19]</sup> and nitrogen reduction reactions.<sup>[20]</sup>

## Acknowledgments

This work was financially supported by the National Natural Science Foundation of China (21922811, 51702284, 21878270, and 21961160742), Zhejiang Provincial Natural Science Foundation of China (LR19B060002 and LR19E080001), the Fundamental Research Funds for the Central Universities, the Startup Foundation for Hundred-Talent Program of Zhejiang University, the Fundamental Research Funds for the Central Universities CCNU20ZT003. We thank BL10B endstation of Hefei Lightsource, BL14W1 beamline in Shanghai and Beijing Synchrotron Radiation Facility (SSRF) for XAS measurements. G. Wu acknowledges the support from National Science Foundation (CBET-1604392, 1804326).

**Keywords:** dynamic understanding • axial traction • single-atom catalyst • electrochemical CO<sub>2</sub>RR

- [1] a) K. Xu, B. Sun, J. Lin, W. Wen, Y. Pei, S. Yan, M. Qiao, X. Zhang, B. Zong, *Nat. Commun.* **2014**, *5*, 5783; b) X. Wang, Q. Zhao, B. Yang, Z. Li, Z. Bo, K.-H. Lam, N. M. Adli, L. Lei, Z. Wen, G. Wu, Y. Hou, *J. Mater. Chem. A* **2019**, *7*, 25191-25202; c) N. Mohd Adli, W. Shan, S. Hwang, W. Samarakoon, S. Karakalos, Y. Li, D. A. Cullen, D. Su, Z. Feng, G. Wang, G. Wu, *Angew. Chem. Int. Ed.* **2020**, doi:10.1002/anie.202012329; d) Y. Zhu, J. Sokolowski, X. Song, Y. He, Y. Mei, G. Wu, *Adv. Energy Mater.* **2020**, *10*, 1902844; e) Q. Shi, S. Hwang, H. Yang, F. Ismail, D. Su, D. Higgins, G. Wu, *Mater. Today* **2020**, *37*, 93-111.
- [2] Y. Wang, H. Su, Y. He, L. Li, S. Zhu, H. Shen, P. Xie, X. Fu, G. Zhou, C. Feng, D. Zhao, F. Xiao, X. Zhu, Y. Zeng, M. Shao, S. Chen, G. Wu, *J. Zeng, C. Wang, Chem. Rev.* **2020**, *120*, 12217-12314.
- [3] J. Qiao, Y. Liu and J. Zhang, *Electrochemical Energy Storage and Conversion: Fundamentals and Technologies*. Boca Raton, Florida: CRC Press. **2016**, 103-154.
- [4] a) Q. Huang, Q. Li, J. Liu, Y. R. Wang, R. Wang, L. Z. Dong, Y. H. Xia, J. L. Wang, Y.-Q. Lan, *Matter* **2019**, *1*, 1656-1668; b) A. Alvarez, M. Borges, J. J. Corral-Perez, J. G. Olcina, L. Hu, D. Cornu, R. Huang, D. Stoian, A. Urakawa, *ChemPhysChem* **2017**, *18*, 3135-3141.
- [5] a) Q. Zhu, X. Sun, D. Yang, J. Ma, X. Kang, L. Zheng, J. Zhang, Z. Wu, B. Han, *Nat. Commun.* **2019**, *10*, 3851; b) S. Ringe, C. G. Morales-Guio, L. D. Chen, M. Fields, T. F. Jaramillo, C. Hahn, K. Chan, *Nat. Commun.* **2020**, *11*, 33.
- [6] a) T. Wang, Q. Zhao, Y. Fu, C. Lei, B. Yang, Z. Li, L. Lei, G. Wu, Y. Hou, *Small Methods* **2019**, *3*, 1900210; b) H. B. Yang, S.-F. Hung, S. Liu, K. Yuan, S. Miao, L. Zhang, X. Huang, H.-Y. Wang, W. Cai, R. Chen, J. Gao, X. Yang, W. Chen, Y. Huang, H. M. Chen, C. M. Li, T. Zhang, B. Liu, *Nat. Energy* **2018**, *3*, 140-147; c) L. Lin, H. Li, C. Yan, H. Li, R. Si, M. Li, J. Xiao, G. Wang, X. Bao, *Adv. Mater.* **2019**, *31*, e1903470.
- [7] a) X. Rong, H. J. Wang, X. L. Lu, R. Si, T. B. Lu, *Angew. Chem. Int. Ed.* **2019**, *59*, 1961-1965; b) R. Jiang, L. Li, T. Sheng, G. Hu, Y. Chen, L. Wang, *J. Am. Chem. Soc.* **2018**, *140*, 11594-11598.
- [8] a) L. Huang, J. Chen, L. Gan, J. Wang, S. Dong, *Sci. Adv.* **2019**, *5*, eaav5490; b) X. Cui, H. Li, Y. Wang, Y. Hu, L. Hua, H. Li, X. Han, Q. Liu, F. Yang, L. He, X. Chen, Q. Li, J. Xiao, D. Deng, X. Bao, *Chem* **2018**, *4*, 1902-1910.
- [9] L. Kong, J. Zhu, W. Shuang, X. H. Bu., *Adv. Energy Mater.* **2018**, *8*, 1801515.
- [10] a) C. Yan, H. Li, Y. Ye, H. Wu, F. Cai, R. Si, J. Xiao, S. Miao, S. Xie, F. Yang, Y. Li, G. Wang, X. Bao, *Energy Environ. Sci.* **2018**, *11*, 1204-1210; b) W. Xiong, J. Yang, L. Shuai, Y. Hou, M. Qiu, X. Li, M. K. H. Leung, *ChemElectroChem* **2019**, *6*, 5951-5957.
- [11] C. Lei, Y. Wang, Y. Hou, P. Liu, J. Yang, T. Zhang, X. Zhuang, M. Chen, B. Yang, L. Lei, C. Yuan, M. Qiu, X. Feng, *Energy Environ. Sci.* **2019**, *12*, 149-156.
- [12] a) W. Zheng, J. Yang, H. Chen, Y. Hou, Q. Wang, M. Gu, F. He, Y. Xia, Z. Xia, Z. Li, B. Yang, L. Lei, C. Yuan, Q. He, M. Qiu, X. Feng, *Adv. Funct. Mater.* **2019**, *30*, 1907658; b) Y. He, X. Zhuang, C. Lei, L. Lei, Y. Hou, Y. Mai, X. Feng, *Nano Today* **2019**, *24*, 103-119.
- [13] X. Li, W. Bi, M. Chen, Y. Sun, H. Ju, W. Yan, J. Zhu, X. Wu, W. Chu, C. Wu, Y. Xie, *J. Am. Chem. Soc.* **2017**, *42*, 14889-14892.
- [14] A. Vasileff, Y. Zheng, S. Z. Qiao, *Adv. Energy Mater.* **2017**, *7*, 1700759.
- [15] J. Li, M. Chen, D. A. Cullen, S. Hwang, M. Wang, B. Li, K. Liu, S. Karakalos, M. Lucero, H. Zhang, C. Lei, H. Xu, G. E. Sterbinsky, Z. Feng, D. Su, K. L. More, G. Wang, Z. Wang, G. Wu, *Nat. Catal.* **2018**, *1*, 935-945.
- [16] K. Yuan, D. F. Lützenkirchen-Hecht, L. Li, L. Shuai, Y. Li, R. Cao, M. Qiu, X. Zhuang, Y. Chen, M. K. H. Leung, U. Scherf, *J. Am. Chem. Soc.* **2020**, *142*, 2404-2412.
- [17] a) Y. Chen, S. Ji, C. Chen, Q. Peng, D. Wang, Y. Li, *Joule* **2018**, *2*, 1242-1264; b) B. Zhang, J. Zhang, J. Shi, D. Tan, L. Liu, F. Zhang, C. Lu, Z. Su, X. Tan, X. Cheng, B. Han, L. Zheng, J. Zhang, *Nat. Commun.* **2019**, *10*, 2980.
- [18] W. Zheng, C. Guo, J. Yang, F. He, B. Yang, Z. Li, L. Lei, J. Xiao, G. Wu, Y. Hou, *Carbon* **2019**, *150*, 52-59.
- [19] a) Y. He, S. Liu, C. Priest, Q. Shi, G. Wu, *Chem. Soc. Rev.* **2020**, *49*, 3484-3524; b) J. Li, H. Zhang, W. Samarakoon, W. Shan, D. A. Cullen, S. Karakalos, M. Chen, D. Gu, K. L. More, G. Wang, Z. Feng, Z. Wang, G. Wu, *Angew. Chem. Int. Ed.* **2019**, *58*, 18971-18980.
- [20] a) S. Mukherjee, X. Yang, W. Shan, W. Samarakoon, S. Karakalos, D. A. Cullen, K. More, M. Wang, Z. Feng, G. Wang, G. Wu, *Small Methods* **2020**, *4*, 1900821; b) H. Xu, K. Ithisuphalap, Y. Li, S. Mukherjee, J. Lattimer, G. Soloveichik, G. Wu, *Nano Energy* **2020**, *69*, 104469.

**Entry for the Table of Contents**

An axial traction strategy is presented to reduce the energy barrier of the dynamic activation process over the M-N<sub>4</sub> structure for boosting CO<sub>2</sub>RR activity.